Modeling of x-ray fluorescence full field imaging using planar square pore micro-channel plate optics

M. Gailhanou, P. Sarrazin, D. Blake

Modeling of X-ray fluorescence full field imaging using planar square pore micro-channel plate optics

M. GAILHANOU[1,*], P. SARRAZIN[2], AND D. BLAKE[3]

[1] Aix Marseille Université, CNRS, IM2NP UMR 7334, 13397 Marseille, France
[2] SETI Institute, Mountain View, CA 94043, USA
[3] NASA Ames Research Center, Moffett Field, CA 94035, USA
[*] Corresponding author: marc.gailhanou@univ-amu.fr

Compiled July 16, 2018

X-ray fluorescence imaging using perfect planar square pore micro-channel plate X-ray optics (MPO) is investigated through the modeling of the MPO point spread function (PSF). A semi-continuous model based on the use of a simplified two parameters reflectivity curve is developed including in particular three kind of contributions. A validation of this model is carried out by calculating variations of several PSF characteristics with the MPO and fluorescence imaging parameters and comparing the results with ray-tracing simulations. A good agreement is found in a large range of X-ray energies; however it is shown that for the lower values of the working distance a discrete model should be used to take into account the periodic nature of the PSF. Ray-tracing simulated images of extended monochromatic sources are interpreted in the light of both the semi-continuous and discrete models. Finally solutions are proposed to improve the imaging properties of MPOs.

OCIS codes: (340.0340) X-ray optics ; 340.7440 X-ray imaging .

http://dx.doi.org/10.1364/ao.XX.XXXXXX

1. INTRODUCTION

Elemental imaging using X-ray fluorescence is a non destructive technique capable of bringing out important information in many fields[1], from materials science to cultural heritage [2–5] and planetary surface analysis [6] . A first class of methods by which X-ray fluorescence images can be obtained consists in the two dimensional scanning of a beam on the object and collection of the fluorescence X-rays at every point of the map [7, 8]. It requires a focusing device and a minimum of two-axis motorized scanner. A second class of methods is based on direct X-ray fluorescence imaging with no moving parts. These direct imaging methods are more suited to situations where mechanical simplicity is critical. Among the different imaging devices that can be used, square-pore micro-channel plate X-ray optics (MPO), sometimes referred to as “Square Multi channel plate optics” , “Multi-pore optics” or “lobster-eye optics” is one of the most attractive because of its efficiency given by the corner cube effect [9–12], in particular when compared with straight polycapillary optics [13, 14] used for 1:1 imaging. Planar MPOs, to which this study will be restricted, offer a magnification of 1 to cover a surface area commensurate with the size of the detector, and provide an additional degree of freedom, compared to spherical MPOs, with the possibility of changing the working distance without changing the magnification.

The understanding of MPO properties relies first on the modeling of perfect structures for which the Chapman et al. publication of 1991 [11] is a reference. The intention of the present publication is to bring several improvements to this model and examine the effect of short distances which are not considered in the work of Chapman et al. The effect of defects related to the manufacturing technology is beyond the scope of our publication with the exception of the modification of reflectivity by surface roughness.

In Chapman et al.[11] two approximations of the reflectivity curve are used, depending on the X-ray energy, and are defined with a single parameter. We will show that a single simplified description might be used with two parameters, the first corresponding to the real part of the reflecting material refractive index and the second related to both absorption (imaginary part of the refractive index) and surface roughness. Using this new simplified curve the behavior of the MPO is much better described in a large range of energies, in particular for heavy reflecting materials like platinum or iridium.

In addition the Chapman et al. model is a continuous model where the pore size is considered as small enough to replace summations by integrals. For this reason the only contributions to the central spot of the PSF considered by Chapman et al. are the ones corresponding to an odd number of reflections in each of the two perpendicular planes containing the pores

faces. It will be shown here that two additional contributions cannot be neglected when the source-MPO distance is decreased. The first additional contribution is related to reflections on the central row and column of pores relative to the optical axis and is visible at medium distance. The second contribution comes from direct transmission by the central pores closest to the optical axis and becomes important only at very small working distances. A new semi-continuous model based on the use of the two-parameter reflectivity curve and taking into account the three contributions mentioned above will be described in the first part of this publication. Using this model the influence of geometrical parameters and X-ray energy on the point spread function (PSF) central spot integrated intensity and profile are shown. The modifications of other features of the PSF such as the two characteristic perpendicular wings and the pseudo-background related in part to the direct transmission through the pores are also investigated.

In the second part it will be shown that the PSF is not unique, it is a periodic function of the source coordinates reflecting the periodicity of the planar MPO itself. It will be shown that the influence of this periodicity is enhanced at small distances and can be reproduced in most cases using a discrete model. The semi-continuous model can however be used in the case of a modified point spread function where a small square with a size (defined as the side length) equal to the pore periodicity is used as a source instead of a point.

Finally in the third part the trends shown in part 2 for the PSF are illustrated by images simulated using ray tracing and improvements to the standard MPO are proposed.

Throughout this publication ray tracing simulations are used to support our modeling because the analysis carried out in this paper is based on geometrical optics. Using the very crude criterion of an angular diffraction contribution on the order of λ/D where λ is the X-ray wavelength and D the pore size we believe that it should be valid in the energy range of the fluorescence of most of the elements and for pore sizes of tens of microns. However it might be necessary to use a wave theory taking into account wave-guide effects, diffraction, eventual interference between pores and the effect of partial coherence for lower energy fluorescence and smaller pore sizes, but it is beyond the scope of this paper.

2. RAY TRACING

Ray tracing simulations (sometimes referred to as Monte Carlo simulations) are used to produce PSFs and quantities which are eventually compared with the results of analytic models. These simulations include the calculation of X-ray reflectivity which is done using the standard matrix method [15]. Anomalous scattering and absorption are taken into account through the calculation of the atomic scattering factor as well as surface and interface roughness through a static Debye-Waller factor with a single parameter which is the root mean square roughness σ. Most of the ray tracing simulations are carried out with a monochromatic point source to obtain the PSF. The remainder use a two dimensional object emitting monochromatic X-rays as a source. The results shown do not depend on the number of rays used, except for the shot noise. The initial number of rays (between 10 million and 1 billion) was, for each kind of simulation, large enough to make the shot noise negligible, or at least not cumbersome. Emission was considered isotropic in the maximum $\pm 0.1 rad$ range used in the simulations.

3. SEMI CONTINUOUS MODEL

The model developed below will be called "semi-continuous" because at some places sums over the pores of the MPO are replaced by integrals (i.e. pores are considered as infinitely small) while at other places the discrete aspect of the MPO is taken into account.

A. Parameters

Figure 1 shows the main geometrical parameters used in the model. In the following D, T and t are respectively the pore size (square side length), the period of the MPO square lattice and the MPO pore length. The distance between the source and the MPO is l_s and is equal to l_i the distance between the MPO and the image plane (see also Figure 15). l_s and l_i are measured with respect to the plane which is half way from the MPO entrance plane and the MPO exit plane. The MPO in-plane dimensions and, as a result, the total number of pores are considered to be infinite, edge effects will not be discussed. Additional material parameters are used through the inner pore coating reflectivity properties.

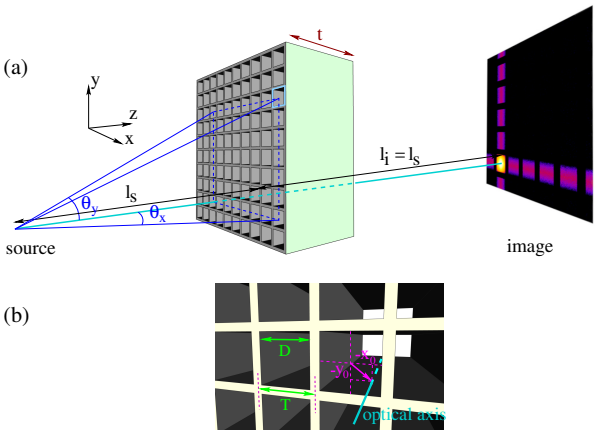

Fig. 1. MPO geometrical parameters (a) Point source imaged in the 1:1 arrangement. (b) Detail showing the precise position (x_0, y_0) of the optical axis with respect to the nearest pore center

B. Reflectivity

In order to enable analytical calculations, a two parameters simplified (linearized) reflectivity curve is used instead of the reflectivity curve calculated using the standard matrix method. (fig. 2). These two parameters are the total reflection critical angle γ_c and $\overline{R}$ the reflectivity averaged between 0 and γ_c. The total reflection critical angle is written as :

$$\gamma_c = \lambda\sqrt{\frac{r_e}{2\pi}N_{\text{av}}\rho_m K} \qquad (1)$$
$$\approx 1.643\,10^{-3}\lambda\sqrt{\rho_m K} \qquad [\gamma_c(rad), \lambda(\text{Å}), \rho_m(g.cm^{-3})]$$
$$K = 2\frac{\sum_i c_i(f_{0i} + f_i'(\lambda))}{\sum_i c_i M_i}$$

where λ is the X-ray wavelength, r_e is the classical electron radius, N_{av} the Avogadro number, ρ_m the mass density, c_i is the element i composition in the reflecting material, $f_{0i} + f_i'(\lambda)$ the element i atomic scattering factor including the anomalous part f', and M_i the element i atomic mass. For light elements the

K coefficient is close to 1, for heavy elements such as Ir or Pt it is around 0.8 and of course for a mixture of light and heavy elements K will be between these values.

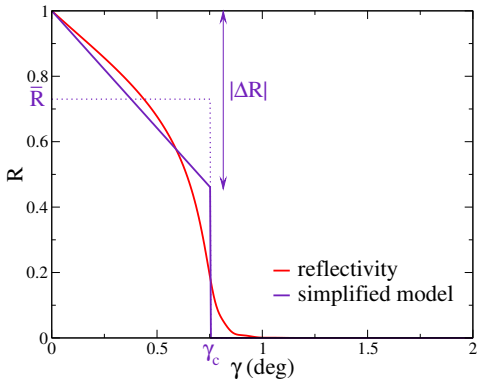

Fig. 2. Example of the simplified version of the reflectivity curve used for analytic calculations (blue line) compared with the simulated reflectivity of an Ir layer on a silica substrate at 6400 eV (red line).

We define $\overline{R}(\lambda)$ by :

$$\overline{R}(\lambda) = \frac{1}{\gamma_c(\lambda)} \int_0^{\gamma_c(\lambda)} R(\gamma,\lambda) d\gamma \qquad (2)$$

where $R(\gamma,\lambda)$ is the reflectivity of the material or stack of materials at the grazing angle γ and X-ray wavelength λ. The value of $\overline{R}(\lambda)$ depends on the surface roughness and on the reflecting material elements atomic scattering factors which themselves depend on energy and can have singular points at X-ray absorption edges. It can be calculated directly by numerical integration of the reflectivity curve. The simplified reflectivity is then given by :

$$\mathcal{R}(\gamma,\lambda) = \begin{cases} 1 + 2(\overline{R}(\lambda) - 1)\gamma/\gamma_c(\lambda) & \gamma \le \gamma_c(\lambda) \\ 0 & \gamma > \gamma_c(\lambda) \end{cases} \qquad (3)$$

When absorption and roughness are low, $\overline{R}(\lambda)$ will be close to 1 and the reflectivity model will be close to the model used by Chapman et al. at high energy. For higher absorption $\overline{R}(\lambda)$ will be close to 0.5 and the simplified reflectivity will be similar to the model used by Chapman at low energy. In the case of medium absorption and roughness - see for example figure 2 - it should work better than the two asymptotic models.

$\gamma_c(\lambda)$ and $\overline{R}(\lambda)$ are the two parameters defining a simplified reflectivity curve. In the calculations it will be however more convenient to use $\Delta R(\lambda)$ instead of $\overline{R}(\lambda)$, with $\Delta R(\lambda) = 2(\overline{R}(\lambda) - 1)$ (figure 2). It might occur, for high absorption and because of the additional effect of roughness, that equation 2 gives a value of $\overline{R}$ lower than 0.5. In this case equation 3 gives negative values for R when γ is close to γ_c. To avoid this, the γ_c value used in the model is replaced by an effective value γ_{ceff} and $\overline{R}$ by $\overline{R}_{eff}$:

$$\overline{R} < 0.5 \begin{cases} \overline{R}_{eff} = 0.5 \\ \gamma_{ceff} = 2\overline{R}\gamma_c \end{cases} \qquad (4)$$

This substitution applies for example in the 2keV-3keV region in the case of Ir for a root mean square (rms) roughness of 2nm, as will be shown later in figure 6.

It appeared that there was a problem with commonly used f' and/or f" tables, such as Henke or Cromer Liberman tables, in the region of M edges of heavy elements such as Ir or Pt, eventually giving negative values of the real part of the atomic scattering factor. For these elements the values published by C.T. Chantler in 2000 [16] were used. Finally we would like to point out that the simplified two parameters analytical approximation of the X-ray reflectivity discussed in this paragraph might be used in grazing incidence applications, beyond the context discussed in this publication.

C. Point spread function (PSF) central spot integrated intensity

A typical simulated MPO point spread function (PSF) is shown on figure 3. The main features are a central spot which is the desirable part for image formation, two perpendicular lines forming a cross and weaker intensity in the quadrants delimited by the cross. All these characteristics parts can be found in experimental PSFs as well [12]. In this section we will calculate Ω_{eff}, the effective solid angle acceptance of the MPO, which multiplied by the source intensity per unit solid angle gives the intensity in a square twice the size the MPO period, i.e. $2T$. The intensity outside this square is not taken into account because it is not properly focused in the image plane.

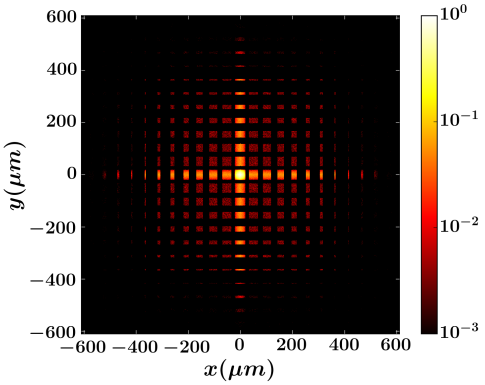

Fig. 3. Ray tracing simulated point spread function (PSF). The reflecting material is a 25nm Ir layer on SiO_2, with a surface and interface roughness both equal to 2nm. $E = 15keV$, $l_s = 0.05m$, $D = 20\mu m$, $T = 26\mu m$, $t = 4.8mm$. Normalized intensity in log scale.

The central spot intensity is usually considered as coming from an odd number of reflections in the two (x,z) and (y,z) planes. At long working distance this contribution is the most significant, however there are two other contributions to the central spot. Figure 4 shows the distribution in the entrance plane of the MPO of the rays contributing to the PSF central spot as a function of the number of reflections in the (x,z) and (y,z) planes noted (n_x, n_y). In this figure, the MPO parameters and the energy of X-rays are such that a maximum of one reflection can occur in each plane. The (odd,odd) reflections - (1,1) in the figure - come from 4 equivalent 2-dimensional regions of the MPO, so this contribution will be named Ω_{2d}. Note that these 4 regions correspond to the 4 regions visible on figure 6 of the Chapman et al. 1991 publication [11]. The second and newly considered contribution is coming from (odd,0) and (0,odd) reflections ((1,0) and (0,1) in the figure) and corresponds to the one or two rows and columns of pores which are the closest to the optical axis.

This contribution will be noted Ω_{1d} as the MPO regions from which it is coming are linear. The last contribution, related to the one to four pores which are the closest to the optical axis, is noted Ω_{0d} as it comes from a very localized region. We have the following relation :

$$\Omega_{\text{eff}} = \Omega_{2d} + \Omega_{1d} + \Omega_{0d}$$

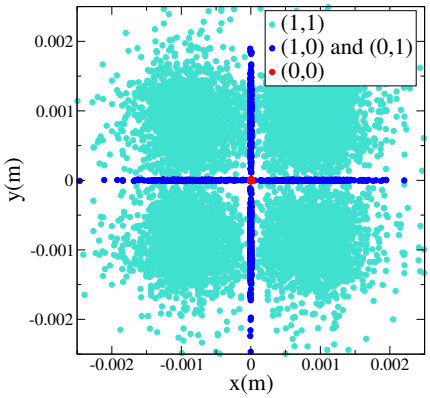

Fig. 4. Distribution of rays, at the entrance surface of the MPO, contributing to the PSF central spot. In the notation (n_x, n_y), n_x is the number of reflections in the xz plane, n_y is the number of reflections in the yz plane. Because of the parameters used here n_x and n_y are either 1 or 0. Parameters : $D = 20\mu m$, $T = 26\mu m$, $t = 1.2mm$, $l_s = 10cm$, $E = 6400eV$, reflective layer: Ir

Ω_{2d} is first calculated with a method close to, and largely inspired by, the method of Chapman et al. [11] using small angle approximations. If $D/l_s \ll \gamma_c$ the rays entering a particular pore of angular position with respect to the source (θ_x, θ_y) (see figure 1a) are considered parallel and their direction is defined by the same angles as the pore angular position. The beam entering this particular pore and that is submitted to n_x reflections in the (x,z) plane and n_y reflections in the (y,z) plane will have a dimension $\delta_{\text{nx}}(\theta_{rx})$ along x and $\delta_{\text{ny}}(\theta_{ry})$ along y. When the number of reflections is greater than 0, $\delta_{\text{nx}}(\theta_{rx})$ and $\delta_{\text{ny}}(\theta_{ry})$ are given by the expression:

$$\frac{\delta_{n_s}(\theta_{rs})}{D} = \begin{cases} 0 & |\theta_{rs}| \le n_s - 1 \\ |\theta_{rs}| - (n_s - 1) & n_s - 1 < |\theta_{rs}| \le n_s \\ n_s + 1 - |\theta_{rs}| & n_s < |\theta_{rs}| < n_s + 1 \\ 0 & |\theta_{rs}| \ge n_s + 1 \end{cases} \quad \textbf{(5)}$$

where the index s will be either x or y and $\theta_{rs} = \theta_s t/D$. In the case where $n_s = 0$:

$$\frac{\delta_0(\theta_{rs})}{D} = \begin{cases} 1 - |\theta_{rs}| & 0 \le |\theta_{rs}| < 1 \\ 0 & |\theta_{rs}| \ge 1 \end{cases} \quad \textbf{(6)}$$

The corresponding effective collected solid angle corresponding to (n_x, n_y) reflection in the same single pore is:

$$\Omega_p(\theta_x, \theta_y) = \frac{\delta_{n_x}(\theta_{rx})\delta_{n_y}(\theta_{ry})}{(l_s - t/2)^2} \mathcal{R}^{n_x}(\theta_x)\mathcal{R}^{n_y}(\theta_y) \quad \textbf{(7)}$$

For infinitely small pores the number of pores in the $d\theta_x d\theta_y$ element of solid angle is :

$$d^2N(\theta_x, \theta_y) = \frac{\eta(l_s - t/2)^2}{D^2} d\theta_x d\theta_y \quad \textbf{(8)}$$

where η is the fraction of the MPO entrance surface occupied by pores. Considering a pore size D and a period of T in both x and y directions:

$$\eta = D^2/T^2$$

The total effective solid angle corresponding to (n_x, n_y) reflections, $\Omega(n_x, n_y)$, is then obtained by integration :

$$\begin{aligned} \Omega(n_x, n_y) &= \int_{\theta_x=-\infty}^{+\infty} \int_{\theta_y=-\infty}^{+\infty} \Omega_p(\theta_x, \theta_y) d^2N(\theta_x, \theta_y) \\ &= 4\eta\gamma_c^2 S_{n_x} S_{n_y} \end{aligned} \quad \textbf{(9)}$$

with

$$S_n = \begin{cases} \frac{1}{\alpha} \int_0^{\alpha} \frac{\delta_n(\theta_{rs})}{D} \mathcal{R}^n(\theta_{rs} t/D)\, d\theta_{rs} & n \ne 0 \\ \frac{1}{2\alpha} & n = 0 \end{cases} \quad \textbf{(10)}$$

where n is either n_x or n_y and:

$$\alpha = t\frac{\gamma_c}{D}$$

Equation 10 is valid for any expression of the reflectivity for which the upper bound, above which reflectivity is equal to zero, is the total reflection critical angle γ_c. It is the case with the simplified reflectivity model of equation 3 which is then used to calculate the integral of equation 10. Writing $\Delta R = 2(\overline{R} - 1)$ and after integration we obtain in the case where $n > 0$:

$$\alpha S_n = \begin{cases} 0 & \alpha \le n - 1 \\ F_n(\Delta R) - F_n((n-1)\Delta R/\alpha) & n - 1 < \alpha < n \\ F_n(n\Delta R/\alpha) - F_n((n-1)\Delta R/\alpha) + & \\ \quad G_n(\Delta R) - G_n(n\Delta R/\alpha) & n \le \alpha < n + 1 \\ F_n(n\Delta R/\alpha) - F_n((n-1)\Delta R/\alpha) + & \\ \quad G_n((n+1)\Delta R/\alpha) - G_n(n\Delta R/\alpha) & \alpha \ge n + 1 \end{cases} \quad \textbf{(11)}$$

where the functions $F_n(U)$ and $G_n(U)$ are defined as follows:

$$\begin{aligned} F_n(U) &= \left(\frac{\alpha}{\Delta R}\right)^2 \left(U\frac{(1+U)^{n+1}}{n+1} - \frac{(1+U)^{n+2}}{(n+1)(n+2)} \right) \\ &\quad - (n-1)\frac{\alpha}{\Delta R}\frac{(1+U)^{n+1}}{n+1} \\ G_n(U) &= \frac{\alpha}{\Delta R}(1+U)^{n+1} \\ &\quad - \left(\frac{\alpha}{\Delta R}\right)^2 \left(U\frac{(1+U)^{n+1}}{n+1} - \frac{(1+U)^{n+2}}{(n+1)(n+2)} \right) \end{aligned}$$

Finally as this contribution to the central PSF spot corresponds to odd numbers of reflections in both xz and yz planes:

$$\Omega_{2d} = 4\eta\gamma_c^2 S_{\text{odd}}^2(\alpha, \Delta R) \quad \textbf{(12)}$$

with :

$$S_{\text{odd}}(\alpha, \Delta R) = \sum_{k=0}^{+\infty} S_{2k+1} \quad \textbf{(13)}$$

Ω_{2d} (equation 12) is proportional to the product of the square of the critical angle and of a function which only depends on α and ΔR. It is important to note that this main contribution to the effective solid angle does not depend on l_s (as will be illustrated later in figure 9) . The reason is that the $1/(ls - t/2)^2$ dependence of the single pore effective solid angle (equation

7) is perfectly compensated by the $(ls - t/2)^2$ dependence of the number of pores involved (equation 8). Figure 5 shows $S_{\text{odd}}(\alpha, \Delta R)$ for a set of values of ΔR going from the maximum value 0 to the minimum value -1, and a range of values of α.

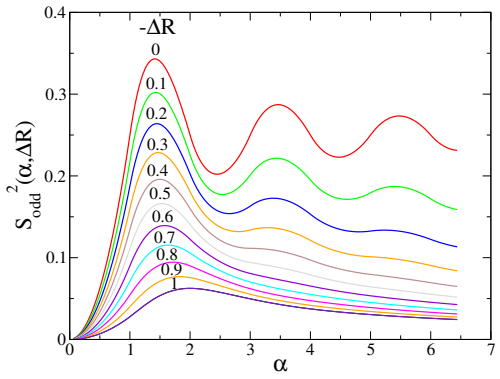

Fig. 5. Plots of $S^2_{\text{odd}}(\alpha, \Delta R)$ as a function of α for different values of ΔR showing the influence of absorption and roughness induced loss on Ω_{2d}

In the paper of Chapman et al. [11] only the extreme cases are considered, $\Delta R = 0$ in the case of high energies and $\Delta R = -1$ for low energies. The refinement brought by the new two parameters reflectivity curve separates the effect of absorption/roughness from the effect of the energy dependent critical angle. In the case of heavy reflecting materials for example, the absorption is neither low nor high in a wide energy range, hence using this 2-parameter reflectivity curve is a necessity.

When considering a particular reflecting material the dependence of ΔR and γ_c with the X-ray energy can be calculated. The example of Ir is shown on figure 6. The refractive index has a simple $1/E$ dependence with the X-ray energy, with the exception of the energy region of the M absorption edges. ΔR is a more complex function of the X-ray energy: it is much more sensitive to the presence of absorption edges such as the Ir L edges in the 11-13 keV range and the M absorption edges in the 2-3 keV range. It is also clearly dependent on the surface root mean square roughness σ. In the 2-3 keV region it was necessary to use effective values of ΔR and γ_c, in the case of Ir with a 2nm rms roughness, calculated using equations 4.

Using the data shown on figure 6, it is possible to plot Ω_{2d} as a function of the X-ray energy on one axis and the ratio t/D on the other axis. The map obtained in the case of an Ir layer with a rms roughness of 2nm is shown in figure 7. This map can be a guide for the choice of the MPO t/D ratio, which will depend on the spectral band of interest. For example large values might be chosen for higher fluorescence energies. As already mentioned there is no dependence of Ω_{2d} on the working distance l_s so for a particular reflecting material all the information on Ω_{2d} is in this map.

The Ω_{1d} contribution to the PSF central spot coming from the row and column of pores shown in dark blue in figure 4. It corresponds to an odd number of reflections in one direction and a direct transmission in the other. A one dimensional integration is carried out in this case, giving for the row in the x direction:

$$\Theta_{1x}(n_x) = \int_{\theta_x=-\infty}^{+\infty} \frac{\sqrt{\eta}(ls - t/2)}{D} \frac{\delta_{n_x}(\theta_{rx})}{(l_s - t/2)} \mathcal{R}^{n_x}(\theta_x) d\theta_x$$
$$= 2\sqrt{\eta}\gamma_c S_{nx}$$

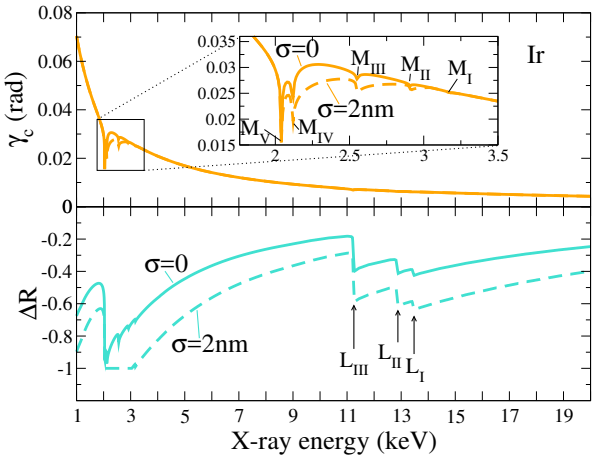

Fig. 6. External total reflection critical angle γ_c and reflectivity loss ΔR as a function of energy in the case of Ir reflective material. ΔR is shown for two values of the root mean square surface roughness σ. The insert shows the 2-3 keV region where effective values γ_{ceff} (equation 4) replace in the case of the 2nm roughness (dotted line) the critical angle value used in the case of a perfect flat surface (continuous line). In this region and in the case of the 2nm rms roughness, $\Delta R = \Delta R_{\text{eff}}$ is constant and equal to -1.

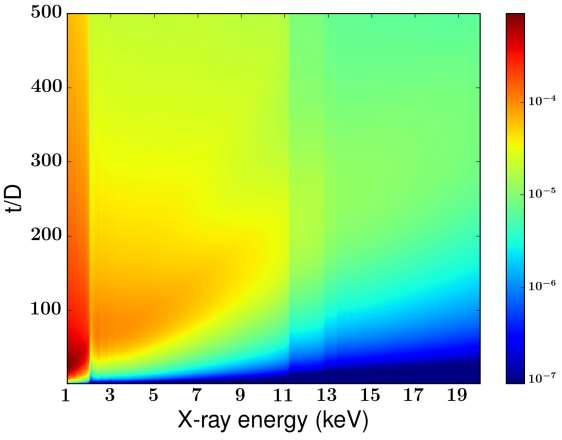

Fig. 7. Ω_{2d} as a function of X-ray energy and t/D in the case of an Ir top layer with a 2nm root mean square roughness. Discontinuities induced by M and L absorption edges of Ir are clearly visible

and an equivalent relation obtained by substitution of x by y for $\Theta_{1y}(n_y)$ corresponding to the column in the y direction. The resulting total solid angle collected by the row and column and focused in the central PSF spot is :

$$\Omega_{1d} = \frac{D}{l_s + t/2} \sum_k \left(\Theta_{1x}(2k+1) + \Theta_{1y}(2k+1)\right) \quad (14)$$

$$= \frac{4D\sqrt{\eta}\gamma_c}{l_s + t/2} S_{odd}(\alpha, \Delta R) = \frac{2D}{l_s + t/2}\sqrt{\Omega_{2d}} \quad (15)$$

Ω_{1d} has a lower dependence to X-ray energy than Ω_{2d} because it depends linearly on γ_c which is roughly proportional to the X-ray wavelength and also because S_{odd} changes with X-ray energy are lower than the changes of S^2_{odd}. Ω_{1d} depends on l_s, shorter distances will increase this contribution.

The last contribution is related to the pinhole-like transmission by the central pore:

$$\Omega_{0d} = \frac{D^2}{(ls + t/2)^2} \quad (16)$$

which shows no spectral dependence and a stronger dependence with the working distance l_s.

Finally the total effective solid angle collection of the MPO is given by:

$$\Omega_{eff} = 4\eta\gamma_c^2 S^2_{odd}(\alpha, \Delta R) + \frac{4D\sqrt{\eta}\gamma_c}{l_s + t/2} S_{odd}(\alpha, \Delta R) + \frac{D^2}{(ls + t/2)^2}$$

$$= \sum_{n=0}^{2} g(n) \left[\sqrt{\eta}\gamma_c S_{odd}(\alpha, \Delta R)\right]^n \left(\frac{D}{l_s + t/2}\right)^{2-n} \quad (17)$$

where g(n) is a kind of degree of degeneracy, $g(n) = 4$ for $n = 1$ or $n = 2$ and $g(0) = 1$. It corresponds to the number of equivalent regions for the three different contributions, which are visible on figure 4.

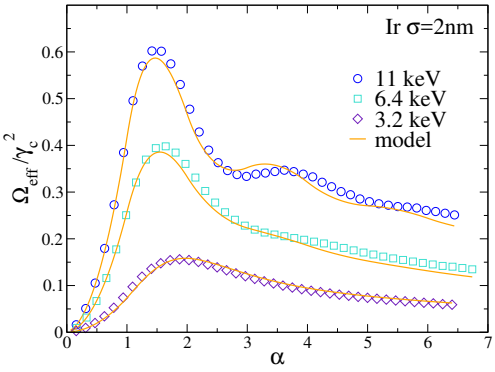

Fig. 8. Ω_{eff}/γ_c^2 as a function of $\alpha = t\gamma_c/D$. Variations of α are obtained, for each energy, by changing the MPO thickness t, D being constant. Ray tracing simulations results (symbols) are compared with the model of equation 17 (continuous lines). Parameters : Ir layer with $\sigma = 2nm$, $l_s = 10cm$, $t = 1.2mm$, $D = 20\mu m$, $T = 26\mu m$.

Ray tracing results are compared in figure 8 with the model of equation 17 in a case where the dominant term in Ω_{eff} is Ω_{2d}, because l_s is large ($l_s = 0.1m$). For this reason the plots of figure 8 are similar to the ones of figure 5. The influence of the two other terms Ω_{1d} and Ω_{0d} is visible on figure 9. Ω_{2d} does not depend on l_s so the l_s dependency of Ω_{eff} clearly visible on this figure is related to Ω_{1d} and Ω_{0d}.

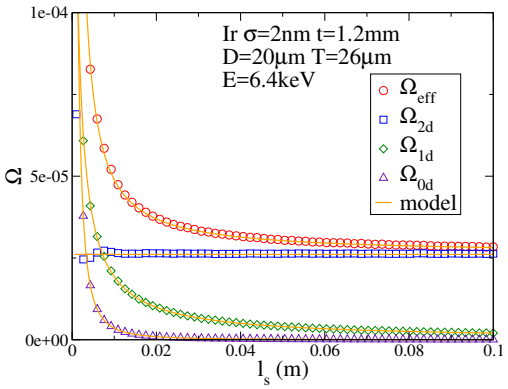

Fig. 9. Ω_{eff}, Ω_{2d}, Ω_{1d} and Ω_{0d} dependence with l_s. Ray tracing simulations results (symbols) are compared with the model of equations 17, 12,14, 16 (continuous lines). Parameters : Ir layer with $\sigma = 2nm$, $t = 1.2mm$, $D = 20\mu m$, $T = 26\mu m$, $E = 6400eV$.

D. PSF central spot profile

The general shape of the central spot is a pyramid, taking the intensity as a third dimension. However, this is the shape related specifically to Ω_{2d}, the two other contributions to the PSF central spot having different profiles. These three profiles can be calculated using the same simplified reflectivity model that was used to determine Ω_{eff}. For this purpose two functions of x or y have to be calculated.

$$P_{1x}(x) = \begin{cases} \dfrac{\sqrt{\eta}\gamma_c}{D'|\Delta R|} \displaystyle\sum_{k=0}^{+\infty} \left[-\frac{(1-U)^{2(k+1)}}{2(k+1)} \right]_{U_{min}(k,x)}^{U_{max}(k,x)} & \dfrac{|x|}{D'} < 1 \\ 0 & \dfrac{|x|}{D'} \geq 1 \end{cases}$$

$$P_{2x}(x) = \begin{cases} \dfrac{1}{2ls} & |x| < D\dfrac{l_s}{l_s + t/2} \\ 0 & \text{otherwise} \end{cases} \quad (18)$$

where

$$D' = \frac{1}{1 - t/(2l_s)} D$$

$$U_{min}(k,x) = (2k + |x|/D')|\Delta R|/\alpha$$

$$U_{max}(k,x) = \min(U_m(k,x), \max(|\Delta R|, U_{min}(k,x)))$$

$$U_m(k,x) = (2(k+1) - |x|/D')|\Delta R|/\alpha$$

The equivalent functions $P_{1y}(y)$ and $P_{2y}(y)$ are obtained by simple substitution of x by y. The three components P_{2d}, P_{1d}, P_{0d} of the profile P_{eff} are then given by:

$$P_{2d}(x,y) = P_{1x}(x)P_{1y}(y)$$

$$P_{1d}(x,y) = P_{1x}(x)P_{2y}(y) + P_{2x}(x)P_{1y}(y)$$

$$P_{0d}(x,y) = P_{2x}(x)P_{2y}(y) \quad (19)$$

The following equation can be used to determine the total effective solid angle in a small $dxdy$ surface element (a detector pixel for example) :

$$d^2\Omega_{eff}(x,y) = P_{eff}(x,y)dxdy$$

$$= (P_{2d}(x,y) + P_{1d}(x,y) + P_{0d}(x,y))dxdy \quad (20)$$

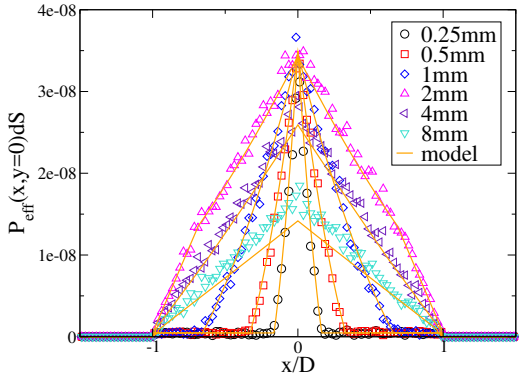

Fig. 10. Central spot profiles for a series of MPO thicknesses t. Ray tracing simulations results (symbols) are compared with the model of equation, 20 (continuous lines). Parameters: $dS = 0.25\mu m^2$, Ir layer with $\sigma = 2nm$, $l_s = 0.1m$, $D = 20\mu m$, $T = 26\mu m$, $E = 6400eV$.

The profiles obtained using equation 20 in the x direction for $y = 0$ are compared with the results of ray tracing simulations in figure 10. This figure shows that the modifications induced in the central spot profile by varying the MPO thickness are well reproduced by the model.

Figure 11 shows the integral breadth (the integrated intensity divided by the maximum intensity, close to the full width at half maximum here) of the central spot in the x (or equivalently y) direction as a function of α for different energies. For $\alpha > 1.5$ the central spot integral breadth is almost constant and equal to the pore size D, while for values between 0 and 1 there is a linear increase of the integral breadth with α. The consequence is that, for a particular MPO thickness, pore size and material, there will be a critical energy below which the central spot size will be constant, and above which it will decrease. We have however to

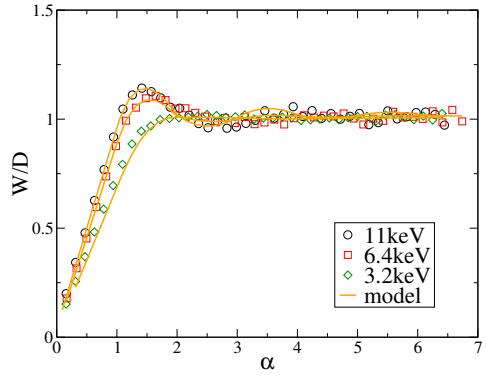

Fig. 11. Central spot x direction profile relative integral breadth W/D as a function of t represented as a function of $\alpha = t\gamma_c/D$ for three different energies : ray tracing simulations results (symbols) and model of equation 20 (continuous lines). Parameters: Ir layer with $\sigma = 2nm$, $l_s = 0.1m$, $D = 20\mu m$, $T = 26\mu m$.

keep in mind that this study focuses on perfect MPO structures, while the central spot profile is sensitive to some MPO defects, in particular the pore orientation dispersion.

E. PSF cross arms and pseudo background

An important feature of the PSF is the presence of a cross centered on the main spot (figure 3). This cross having detrimental effects on image resolution, it is interesting to see how its intensity and reach, which should be both minimized, is influenced by instrumental parameters. It is however a complex task because the PSF cross arms result from the concentration of all the rays undergoing an odd number of reflections in one direction (x or y) and their dispersion in the other direction because of an even number of reflections (including 0). Furthermore the intensity and eventually the reach of the cross arms in the region around the PSF central spot depend on the direct transmission by the MPO, which is a purely geometrical factor, and on the reflectivity which changes with the material and X-ray energy.

To evaluate the effect of PSF cross arms, we will use three quantities: Ω_{arms} the integrated cross arms intensity, Ω_{arms0} the intensity of the cross arms close to the PSF central spot corresponding to (odd,0) and (0,odd) reflections, and the local cross arm intensity within the central spot estimated using $\Omega_{1\text{d}}$ (equation 14). The two first quantities can be calculated using equations 9, 10 and 11:

$$\Omega_{\text{arms}} = 8\eta\gamma_c^2 S_{\text{even}}(\alpha,\Delta R)S_{\text{odd}}(\alpha,\Delta R) - \Omega_{1d} \quad \textbf{(21)}$$

$$\Omega_{\text{arms0}} = 4\eta\frac{\gamma_c^2}{\alpha}S_{\text{odd}}(\alpha,\Delta R) - \Omega_{1d} \quad \textbf{(22)}$$

In these two expressions Ω_{1d} is subtracted from the cross arms intensity because it is considered as a part of the PSF central spot. This subtraction can be neglected if $l_s \gg D\sqrt{\Omega_{2\text{d}}}$. S_{odd} and S_{even} are defined by equations 13 and 23, respectively.

$$S_{\text{even}}(\alpha,\Delta R) = \sum_{k=0}^{+\infty} S_{2k} \quad \textbf{(23)}$$

The following part is restricted to the case where $l_s \gg D\sqrt{\Omega_{2\text{d}}}$. To evaluate the cross arms intensity relative to the intensity of the central spot, we can calculate the ratio :

$$\frac{\Omega_{\text{arms}}}{\Omega_{\text{eff}}} \approx \frac{\Omega_{\text{arms}}}{\Omega_{2\text{d}}} = 2\frac{S_{\text{even}}}{S_{\text{odd}}} \quad \textbf{(24)}$$

$$\frac{\Omega_{\text{arms0}}}{\Omega_{\text{eff}}} \approx \frac{\Omega_{\text{arms0}}}{\Omega_{2\text{d}}} = \frac{1}{\alpha S_{\text{odd}}} \quad \textbf{(25)}$$

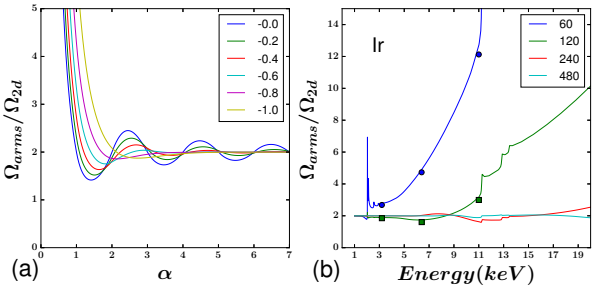

Fig. 12. $\Omega_{\text{arms}}/\Omega_{2\text{d}}$: (a) as a function of α for values of ΔR in the range 0 to -1, (b) as a function of energy for different values of t/D, (60,120,240,480), in the case of an Ir layer with a 2nm surface rms roughness. Continuous lines are obtained using equation 24, symbols are results from ray tracing simulations.

Figure 12(a) shows that, for $\alpha > 2$, the ratio of the cross arms intensity over the central spot intensity is roughly constant

while it increases sharply when α is reduced below 1. Given fixed values of t/D and a particular reflecting material, α and ΔR will only depend on the X-ray energy. As a result, it is possible to plot the cross arms relative intensity as a function of the energy. Figure 12(b) shows that in the case of an Ir reflecting surface with a 2nm RMS roughness a t/D ratio in the 200-400 range will give small changes in this relative intensity over a 3-20 keV range. It is a t/D range where Ω_{2d} changes are also minimized as it was shown on figure 7.

The last contribution to the PSF is the direct transmission and rays undergoing (even,even) reflections, called pseudo-background for its 2-dimensional nature as opposed to the 0-dimensional central spot and 1-dimensional cross arms. The ratio between its integrated intensity and the central spot intensity when $l_s \gg D\sqrt{\Omega_{2d}}$ is written as:

$$\frac{\Omega_{\text{p.background}}}{\Omega_{\text{eff}}} \approx \frac{\Omega_{\text{p. background}}}{\Omega_{2\text{d}}} = \frac{S^2_{\text{even}}}{S^2_{\text{odd}}} = \frac{1}{4}\left(\frac{\Omega_{\text{arms}}}{\Omega_{2\text{d}}}\right)^2 \quad (26)$$

Large values of $\Omega_{\text{arms}}/\Omega_{2\text{d}}$ will correspond to even larger values of $\Omega_{\text{p. background}}/\Omega_{2\text{d}}$ as this ratio is always greater than one.

The reach of the cross and pseudo background is:

$$W_{\text{cross}} = \max(4l_sD/t, 4l_s\gamma_c)$$

It is proportional to l_s and depends on the X-ray energy below a critical energy influenced by reflecting material and D/t (see figure 13 in the case of Ir). The size of the cross and pseudo-

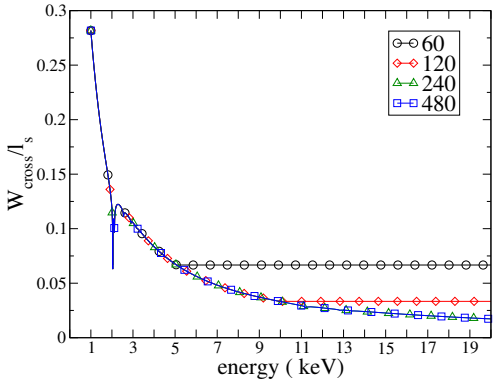

Fig. 13. Relative reach of the cross and pseudo background as a function of X-ray energy for t/D ratios ranging from 60 to 480

background region tends to be higher at low energy, but their intensity with respect to the central spot intensity tends to be lower. Figure 13 also shows that lower values of the cross arms and pseudo background reaches are obtained with higher values of the t/D ratio.

4. DISCRETE MODEL AND SEMI-CONTINUOUS MODEL IN THE CASE OF SHORT l_s DISTANCES

For decreasing values of l_s, some situations result in a limited number of pores contributing to the PSF and, as a consequence, integrations have to be replaced by discrete sums over the pores and integrations within each pore. For these lower l_s values the periodic nature of the PSF is more visible as shown in an extreme case in figure 14.

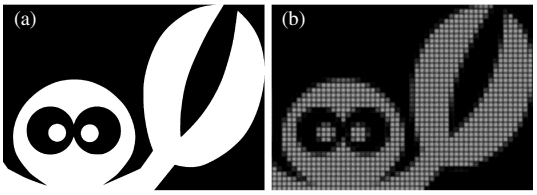

Fig. 14. Ray tracing simulation showing the enhancement of the periodic nature of the MPO point spread function at short distance (a) Source. (b) Image showing a periodic modulation at places where the source is uniform . Reflective material : Ir. $E = 6400eV$, $l_s = 1.2mm$, $D = 20\mu m$, $t = 1.2mm$

Let us consider the pore (i,j) at a distance (x_i, y_j) from the optical axis, with $x_i = x_0 + iT$ and $y_j = y_0 + jT$. $-x_0$ and $-y_0$ are the coordinates of the optical axis in the plane of the MPO with respect to the center of the nearest pore (see figure 1 (b)). Restricting first the analysis to the (xz) plane (see figure 15), its angular position θ_i and angular aperture $\Delta\theta$ can be written as:

$$\theta_i = \frac{|x_i|}{l_s - t/2}$$
$$\Delta\theta = \frac{D}{l_s - t/2}$$

The minimum and maximum angles of the rays entering in the pore i are, as illustrated in figure 15 and in the case where $i \neq 0$:

$$\theta_{\min}(i) = \theta_i - \Delta\theta/2$$
$$\theta_{\max}(i) = \theta_i + \Delta\theta/2$$

The case of $i = 0$ is a little bit more complicated. If $|x_0| \geq D/2$ the formula above apply. In the case where $|x_0| < D/2$ the optical axis is inside the pore, and we split the pore in two parts, noted with the exponents + and -, with :

$$\theta^+_{\min}(0) = 0$$
$$\theta^+_{\max}(0) = \theta_i + \Delta\theta/2$$
$$\theta^-_{\min}(0) = 0$$
$$\theta^-_{\max}(0) = -\theta_i + \Delta\theta/2$$

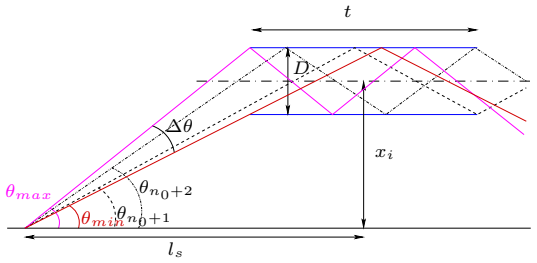

Fig. 15. Side view of a channel with the distances and angles used in the discrete model

From $\theta_{\min}(i)$ and $\theta_{\max}(i)$, the minimum and maximum num-

bers of reflections of rays entering the pore i can be calculated:

$$n_{\min}(i) = \left\lfloor \frac{\theta_{\min}(i)t}{D} \right\rfloor$$
$$n_{\max}(i) = \left\lfloor \frac{\theta_{\max}(i)t}{D} \right\rfloor + 1$$

where the symbols $\lfloor\ \rfloor$ indicates the floor integer value. For a particular position of pore x_i and a particular number of reflections $n \neq 0$ in the (xz) plane, the effective source angular range going through the pore can be written as :

$$\Delta\theta_{\text{eff}}(n, x_i) = \int_{\theta_1}^{\theta_2} R^n(\lambda, \gamma) d\gamma = \frac{\gamma_c}{\Delta R} \left[\frac{(1+U)^{n+1}}{n+1} \right]_{\Delta R\theta_1/\gamma_c}^{\Delta R\theta_2/\gamma_c} \quad (27)$$

where

$$\theta_1, \theta_2 = \begin{cases} \min(\theta_{\min}, \gamma_c), \min(\theta_{x_i}(n_{\min}+1), \gamma_c) & n = n_{\min} \\ \min(\theta_{x_i}(n), \gamma_c), \min(\theta_{x_i}(n+1), \gamma_c) & n_{\min} < n < n_{\max} \\ \min(\theta_{x_i}(n_{\max}), \gamma_c), \min(\theta_{\max}, \gamma_c) & n = n_{\max} \end{cases}$$

with :

$$\theta_{x_i}(n) = \frac{1}{l_s + t/2} \left[|x_i| + (n - 1/2)D \right]$$

As opposed to the continuous model the ray angle and the reflectivity changes within a single pore are taken into account. Similar equations can be written for reflections in the (yz) plane and the pore position y_i, simply replacing x by y.

Using the approximated expression of reflectivity of equation 3 for the integrals of equations 27, two quantities are then calculated :

$$\Sigma_{\text{x,odd}} = \sum_{i=-\infty}^{+\infty} \sum_{k=0}^{+\infty} \Delta\theta_{\text{eff}}(2k+1, x_i)$$
$$\Sigma_{\text{y,odd}} = \sum_{j=-\infty}^{+\infty} \sum_{k=0}^{+\infty} \Delta\theta_{\text{eff}}(2k+1, y_j)$$

In each of the sums over the pores (indices i and j) the eventual splitting of the central pore in two parts, along x and/or y direction, has to be taken into account.

Two other quantities are necessary for the full calculation corresponding to the part of the direct transmission which reaches the image plane at $(\Delta x, \Delta y)$ from the optical axis, with $|\Delta x| \leq D$ and $|\Delta y| \leq D$.

$$\Sigma_{\text{x,0}} = \sum_{k,\ n_{minx}=0} \left[\min(\theta_{x_k}(1), D/(2l_s)) - \min(\theta_{\text{min-xk}}, D/(2l_s)) \right]$$
$$\Sigma_{\text{y,0}} = \sum_{k,\ n_{miny}=0} \left[\min(\theta_{y_k}(1), D/(2l_s)) - \min(\theta_{\text{min-yk}}, D/(2l_s)) \right]$$

The sums are carried out over the pores for which the minimum number of reflections in each plane is equal to 0, and take again into account the eventual splitting of the central pore in two or four parts. The effective collected solid angle then becomes :

$$\Omega_{\text{effective,d}} = (\Sigma_{\text{x,odd}} + \Sigma_{\text{x,0}})(\Sigma_{\text{y,odd}} + \Sigma_{\text{y,0}}) \quad (28)$$

This discrete model was tested first by comparing the intensity profile obtained using ray tracing by moving the MPO along the x direction, changing x_0, with y_0 equal to 0 to the one

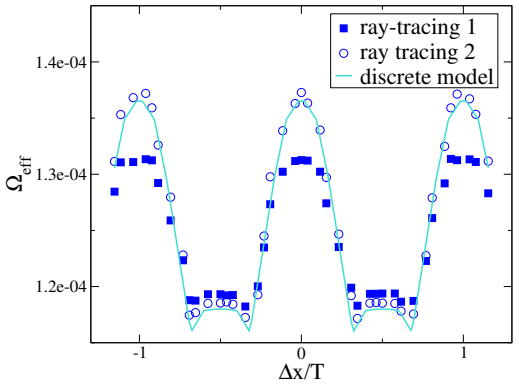

Fig. 16. Ω_{eff} as a function of x for $y = 0$. The continuous line was calculated using equation 28. The first series of ray tracing simulations was carried out using the simplified reflectivity curve (circles), the second series using the real reflectivity (squares). The x profile is quite sensitive to the exact reflectivity profile. Parameters : Ir, energy $= 6400eV, \sigma = 2nm$, $l_s = 5mm, t = 2.4mm$, $D = 20\mu m$, $T = 26\mu m$.

obtained using equation 28 (figure 16) . Two sets of ray tracing simulations were carried out, the first set (ray tracing 1 on the figure) using the exact reflectivity curve while the second set (ray tracing 2 on the figure) used the approximated curve. The points obtained using this second set are very close to the model demonstrating that the quantitative differences observed between the model and the first set are related to the shape of the reflectivity curve used in the model.

As the approximated reflectivity is closer to the real reflectivity when absorption is lower, it is expected that the discrete model works better at higher energies. Figure 17 shows that the two kinds of ray tracing simulations give almost the same results above 10keV and are very close to the discrete model. Below that value there are visible differences. The difference between the discrete model and the ray tracing of type 2 comes from the fact that, at low values of l_s and at low energy, other combinations of reflections than the ones considered in the model should be taken into account. At larger distances the rays undergoing these combinations of reflections are not reaching the central PSF spot. When $l_s = t/2$ every ray that is not absorbed contributes to the central spot which is actually the whole PSF. For intermediate and short values of l_s a part of these rays will be in the central spot. We did not try to make a model for these specific situations, leaving them to ray tracing.

A. Validity of the semi-continuous model at short distance l_s when using a square source

Although simulations with a point source and the discrete model presented above are useful in showing the modulation of the PSF with the source position, it is interesting with respect to fluorescence imaging to know the PSF averaged over the MPO unit cell. It can be obtained using a source emitting uniformly over a square of size T (the MPO period), and it can be shown that it is equivalent to the integration of the semi-continuous model. If N_s is the total number of photons emitted by this source in the 4π solid angle, the number of photons emitted in the solid angle element $d\Omega$ by the surface element of the source dS is:

$$d^4n = \frac{N_s}{4\pi T^2} dS d\Omega = \frac{N_s \eta}{4\pi D^2} dS d\Omega$$

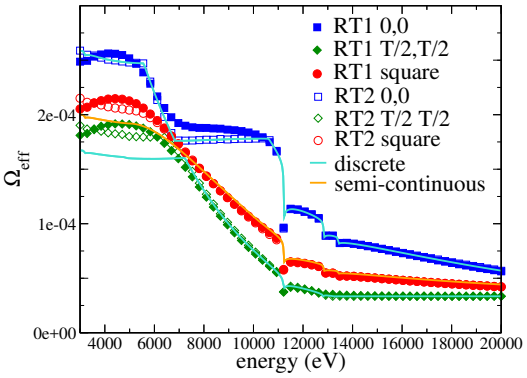

Fig. 17. Ω_{eff} as a function the X-ray energy in the case of a short l_s distance. RT1 and RT2 are ray tracing simulations using two kinds of reflectivity curves (see text). These ray tracing simulations were done using a point source at $x = 0$,$y = 0$ (square symbols), a point source at $x = T/2$,$y = T/2$ (diamond symbols) or a uniform square source of side length T (circle symbols). The ray tracing simulations are compared with the discrete and the semi-continuous model (lines). Parameters : Ir, $l_s = 2.5mm$, $\sigma = 2nm$, $t = 2.4mm$, $D = 20\mu m$, $T = 26\mu m$.

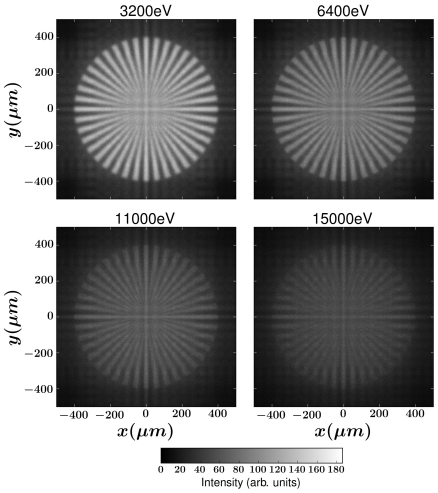

Fig. 18. Ray-tracing simulations of a Siemens star imaged at different energies using an MPO for a relatively large distance $l_s = l_i = 100mm$. MPO parameters : Ir with a 2nm rms roughness as reflecting material, pore size $D = 20\mu m$, period $T = 26\mu m$, thickness $1.2mm$. The number of rays generated and the intensity scale are the same for the four simulations.

Because of the source size, for any source-MPO distance l_s and any pore size D, a full pore will be illuminated in any direction (θ_x, θ_y). In this direction the element of surface of the source providing photons undergoing (n_x, n_y) reflections will be exactly $dS = \delta_{\text{nx}}(\theta_x)\delta_{\text{ny}}(\theta_y)$ that can be calculated using equations 5 and 6. At the exit of the MPO, the number of photons, incoming in the solid angle $d\Omega = d\theta_x d\theta_y$ at angles (θ_x, θ_y) and having experienced (n_x, n_y) reflections, is given by:

$$d^2n = \delta_{nx}(\theta_{rx})\delta_{ny}(\theta_{ry})\mathcal{R}^{n_x}(\theta_x)\mathcal{R}^{n_y}(\theta_y)\frac{N_s\eta}{4\pi D^2}d\theta_x d\theta_y$$

If we calculate this quantity for $N_S/(4\pi)$ equal to 1, we find the product $\Omega_p(\theta_x, \theta_y)d^2N(\theta_x, \theta_y)$ of the two quantities given by equations 7 and 8. We obtain the important result that even for a short working distance equation 17 remains valid with an extended square source having for size the MPO period T. The local variations of the PSF can only be predicted by a discrete model, but the average over a MPO period can be calculated using the semi-continuous model.

The comparison of ray tracing simulations using a square source (figure 17, red circle symbols) with the semi-continuous model shows a good agreement at a low l_s distance - except at low energy for the reason exposed above in the case of a point source.

5. IMAGING

We have examined in details and explained the influence of the parameters of an MPO imaging experiment on the MPO point spread function using two different models. This section aims to show that the trends outlined in this analysis are visible when imaging extended objects. For that purpose, a Siemens star and a regular grid are used as monochromatic extended X-ray sources in ray-tracing simulations.

Figure 18 shows images of a Siemens star obtained at different energies. The most visible feature is the decrease in intensity when increasing energy, which is predicted by equation 12 and illustrated in figure 7. At each energy a cross is visible in the central part of the image, it is directly connected to the PSF cross seen on figure 3. The effect of the cross is also noticeable in the region outside of the circle containing the Siemens star, creating a background intensity which does not change substantially when increasing energy. It means that the contrast is decreasing with energy, in agreement with equation 24 which predicts an increase with energy in the ratio between the cross integrated intensity and the central spot intensity.

Figure 19 shows the increase in intensity when decreasing $l_s = l_i$ as predicted by equation 17 and illustrated by figure 9. For the lower distances the spatial dependence of the PSF explained by the discrete model (equation 28) is more and more visible.

Finally figure 20 is an illustration of the dependence of the central spot size - and thus image resolution - with the MPO t/D ratio predicted by equation 20 and illustrated by figures 10 and 11. Two grid orientations are used : the numerical experiment shows that the grid starts to be visible for higher MPO thicknesses when the grid is parallel to the MPO square array than when it is at 45 degrees because of the anisotropy of the PSF. We remind the reader that MPO are considered as perfect in this publication and that the relatively high resolution predicted in some cases might be difficult to achieve due to pores imperfect orientations or slope errors. Figure 20 is also an illustration of the increase in the ratio between the PSF cross integrated intensity and the PSF central spot that might occur when decreasing the ratio t/D.

6. PROPOSED IMPROVEMENTS

Two features of the PSF have a negative impact when using MPO for imaging: the cross related to odd/even reflections on adjacent pore sides and the PSF spatial dependence. The cross might be transformed in a more isotropic feature by two different means. The first approach involves an array of square

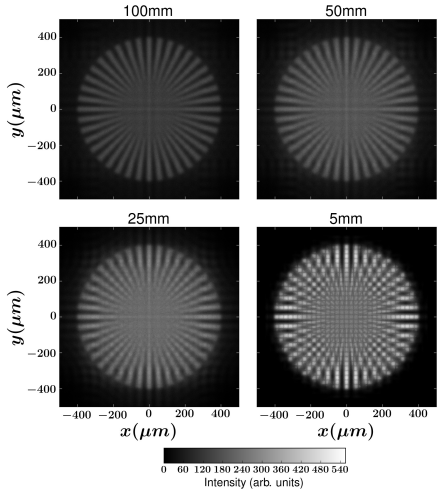

Fig. 19. Ray-tracing simulations of the MPO imaging of a Siemens star for different distances $l_s = l_i$. MPO parameters : Ir with a 2nm rms roughness is the reflecting material, X-ray energy is 6400eV, pore size $D = 20\mu m$, period $T = 26\mu m$, thickness $2.4mm$. The number of rays generated and the intensity scale are the same for the four simulations.

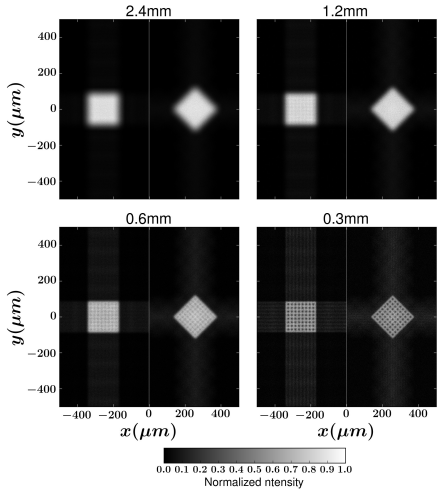

Fig. 20. Ray tracing simulations of a grid imaged with MPOs of different thicknesses. For each MPO thickness two images with a different grid orientation (0 degree and 45 degree) are shown. The pitch of the grid is 10 microns, the holes are squares with a side length of 5 microns. MPO parameters : Ir with a 2nm rms roughness is the reflecting material, X-ray energy is 6400eV, pore size $D = 20\mu m$, period $T = 26\mu m$. The intensity is normalized for each image.

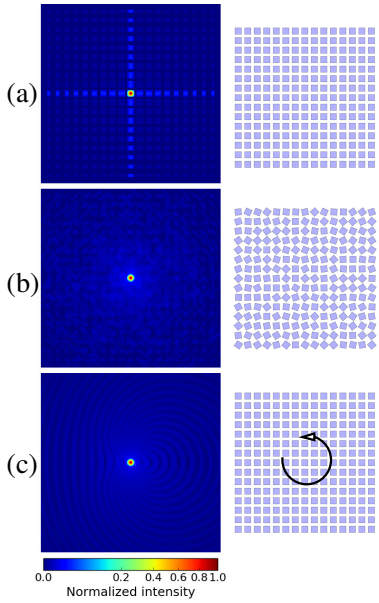

Fig. 21. Ray-tracing simulations of the MPO point spread function. (a) using a standard MPO with a fixed orientation. (b) using a modified static MPO with a random orientation of the pores square cross section. (c) a standard MPO with a continuous rotation. The rotation axis is parallel to the pore axis with a position at 150 microns from the PSF center. MPO parameters : $l_s = l_i = 100mm$,Ir with a 2nm rms roughness is the reflecting material, pore size $D = 20\mu m$, period $T = 26\mu m$, thickness $1.2mm$. The number of rays generated and the intensity scale are the same for the three simulations.

pores with a random orientation of the square cross section. This pore packing scheme was already proposed by R. Willingale et al. [17] as well as other pore orientation patterns for the BEPICOLUMBO spectrometer. As outlined in this reference the pore open fraction η has to be reduced in this case, the consequence being an overall reduction of the intensity of all the parts of the PSF. The second method consists in a rotation of a regular MPO, precise enough to achieve a negligible precession of the PSF. Figure 21 shows the PSF resulting from these two kind of modifications (labeled b and c, respectively) compared to the regular MPO PSF (a). In the case of the rotation the results depend on the position of the rotation axis, but changing this position gives similar results. Both new configurations are quite efficient in making the PSF more isotropic.

The efficiency of the two modified configurations are evaluated by imaging a Siemens star (figure 22). It is interesting to see that both configurations have a similar effect at large distance (100 mm here), but that only the rotation provides a good result at short distance (5mm here). As a matter of fact the image obtained using the randomly oriented squares is not very different at short distance than the image obtained using a regular MPO. This can be explained by the limited number of channels involved for each point of the extended source, which is also the origin of the periodicity of the PSF discussed above in the case of a regular MPO.

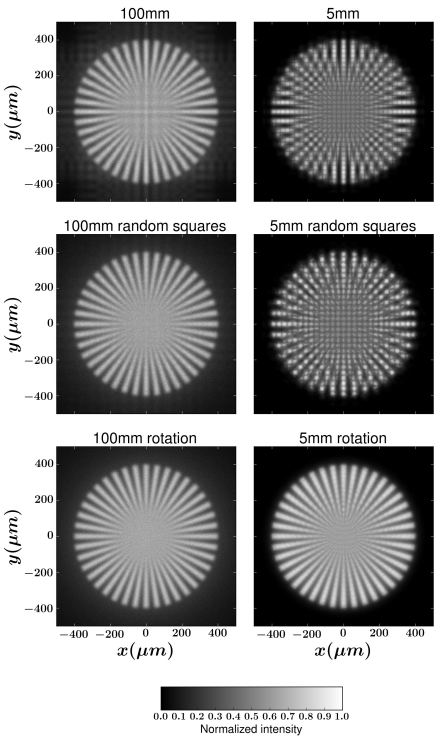

Fig. 22. Effect of a random square orientation (central row) or a MPO rotation (bottom row) on imaging for two working distances (100mm, left column and 5mm, right column), compared to the standard MPO (top row). MPO parameters : Ir with a 2nm rms roughness is the reflecting material, pore size $D = 20\mu m$, period $T = 26\mu m$, thickness $1.2mm$. The intensity is normalized for each image.

7. CONCLUSION

Analytical expressions of the main PSF features of perfect planar MPOs were obtained using a semi-continuous model. This model is based on a two parameters approximation of the X-ray reflectivity curve and takes into account two contributions which were not considered in previous models. It was validated against results of ray tracing simulations by varying several parameters of a X-ray fluorescence imaging experiment: MPO parameters such as the thickness and ratio between the pore size and the thickness, and experimental parameters such as X-ray energy and working distance. The benefit of this analytical model is to evidence the influence of these parameters on the intensity and spatial resolution of an X-ray fluorescence experiment. It was also shown that, for short distances, it is necessary to use a discrete model which has however the disadvantage of clouding the influence of the different parameters.

Series of images of extended sources such as a Siemens star or a grid are interpreted in the light of the semi-continuous and the discrete models we have developed and solutions are also proposed to improve the quality of these images through an isotropization of the PSF.

Finally, it is worth noting that real MPOs show imperfections that might add another level of complexity to this analysis and bring important modifications to the behavior of MPOs [18]. These imperfections were purposely not considered here because it appeared necessary to first establish precise models of a perfect MPO.

8. FUNDING INFORMATION

NASA MatISSE16_2-0005

REFERENCES

1. K. Tsuji, T. Matsuno, Y. Takimoto, M. Yamanashi, N. Kometani, Y. C. Sasaki, T. Hasegawa, S. Kato, T. Yamada, T. Shoji, and N. Kawahara, "New developments of x-ray fluorescence imaging techniques in laboratory," Spectrochimica Acta Part B: Atomic Spectroscopy **113**, 43 – 53 (2015).
2. M. Alfeld, K. Janssens, J. Dik, W. de Nolf, and G. van der Snickt, "Optimization of mobile scanning macro-xrf systems for the in situ investigation of historical paintings," J. Anal. At. Spectrom. **26**, 899–909 (2011).
3. I. Reiche, K. Müller, M. Albéric, O. Scharf, A. Wähning, A. Bjeoumikhov, M. Radtke, and R. Simon, "Discovering vanished paints and naturally formed gold nanoparticles on 2800 years old phoenician ivories using sr-ff-microxrf with the color x-ray camera," Analytical Chemistry **85**, 5857–5866 (2013). PMID: 23662905.
4. L. Bertrand, L. Robinet, M. Thoury, K. Janssens, S. X. Cohen, and S. Schöder, "Cultural heritage and archaeology materials studied by synchrotron spectroscopy and imaging," Applied Physics A **106**, 377–396 (2012).
5. P. Walter, P. Sarrazin, M. Gailhanou, D. Hérouard, A. Verney, and D. Blake, "Full-field xrf instrument for cultural heritage: Application to the study of a caillebotte painting," X-Ray Spectrometry **online doi:10.1002/xrs.2841** (2018).
6. D. Blake, P. Sarrazin, T. Bristow, R. Downs, M. Gailhanou, F. Marchis, D. Ming, R. Morris, V. A. Solé, K. Thompson, P. Walter, M. Wilson, A. Yen, and S. Webb, "The mapping x-ray fluorescence spectrometer (mapx)," 3rd International Workshop on Instrumentation for Planetary Missions (2016). Abstr. 4006.
7. R. Alberti, T. Frizzi, L. Bombelli, M. Gironda, N. Aresi, F. Rosi, C. Miliani, G. Tranquilli, F. Talarico, and L. Cartechini, "Crono: a fast and reconfigurable macro x-ray fluorescence scanner for in-situ investigations of polychrome surfaces," X-Ray Spectrometry **46**, 297–302 (2017). XRS-16-0094.R1.

8. F. P. Romano, C. Caliri, P. Nicotra, S. Di Martino, L. Pappalardo, F. Rizzo, and H. C. Santos, "Real-time elemental imaging of large dimension paintings with a novel mobile macro x-ray fluorescence (ma-xrf) scanning technique," J. Anal. At. Spectrom. **32**, 773–781 (2017).
9. J. R. P. Angel, "Lobster eyes as x-ray telescopes," Astrophysical Journal **233**, 364–373 (1979).
10. G. J. Price, G. W. Fraser, J. F. Pearson, J. P. Nussey, I. B. Hutchinson, A. D. Holland, K. Turner, and D. Pullan, "Prototype imaging x-ray fluorescence spectrometer based on microchannel plate optics," Review of Scientific Instruments **75**, 2314–2319 (2004).
11. H. N. Chapman, K. A. Nugent, and S. W. Wilkins, "X-ray focusing using square channel-capillary arrays," Review of Scientific Instruments **62**, 1542–1561 (1991).
12. P. Sarrazin, D. Blake, M. Gailhanou, F. Marchis, C. Chalumeau, S. Webb, P. Walter, E. Schyns, K. Thompson, and T. Bristow, "Mapx: 2d xrf for planetary exploration - image formation and optic characterization," Journal of Instrumentation **13**, C04023 (2018).
13. H. N. Chapman, K. A. Nugent, and S. W. Wilkins, "X-ray focusing using cylindrical-channel capillary arrays. i. theory," Appl. Opt. **32**, 6316–6332 (1993).
14. F. P. Romano, C. Caliri, L. Cosentino, S. Gammino, D. Mascali, L. Pappalardo, F. Rizzo, O. Scharf, and H. C. Santos, "Micro x-ray fluorescence imaging in a tabletop full field-x-ray fluorescence instrument and in a full field-particle induced x-ray emission end station," Analytical Chemistry **88**, 9873–9880 (2016). PMID: 27656755.
15. J. Daillant and A. Gibaud, eds., *X-ray and neutron reflectivity, theory and applications* (Springer, 1999), chap. 3 Specular reflectivity from smooth and rough surfaces.
16. C. T. Chantler, "Detailed tabulation of atomic form factors, photoelectric absorption and scattering cross section, and mass attenuation coefficients in the vicinity of absorption edges in the soft x-ray (z=30–36, z=60–89, e=0.1 kev–10 kev), addressing convergence issues of earlier work," Journal of Physical and Chemical Reference Data **29**, 597–1056 (2000).
17. R. Willingale, G. W. Fraser, and J. F. Pearson, "Optimization of square pore optics for the x-ray spectrometer on bepi-columbo," Proc.SPIE **5900**, 590012 (2005).
18. R. Willingale, J. F. Pearson, A. Martindale, C. H. Feldman, R. Fairbend, E. Schyns, S. Petit, J. P. Osborne, and P. T. O'Brien, "Aberrations in square pore micro-channel optics used for x-ray lobster eye telescopes," Proc. of SPIE **9905** (2016).